OPEN ACCESS

First Cycle Cracking Behaviour Within Ni-Rich Cathodes During High-Voltage Charging

Journal of The Electrochemical Society, 2023 **170** 070513

First Cycle Cracking Behaviour Within Ni-Rich Cathodes During High-Voltage Charging

A. Wade,[1,2,=] A. V. Llewellyn,[1,2,=] T. M. M. Heenan,[1,2] C. Tan,[1,2] D. J. L. Brett,[1,2] Rhodri Jervis,[1,2] and P. R. Shearing[1,2,z]

[1]*Electrochemical Innovation Lab, Department of Chemical Engineering, UCL, London WC1E 7JE, United Kingdom*
[2]*The Faraday Institution, Quad One, Harwell Science and Innovation Campus, Didcot, OX11 0RA, United Kingdom*

Increasing the operating voltage of lithium-ion batteries unlocks access to a higher charge capacity and therefore increases the driving range in electric vehicles, but doing so results in accelerated degradation via various mechanisms. A mechanism of particular interest is particle cracking in the positive electrode, resulting in losses in capacity, disconnection of active material, electrolyte side reactions, and gas formation. In this study, NMC811 ($LiNi_{0.8}Mn_{0.1}Co_{0.1}O_2$) half-cells are charged to increasing cut-off voltages, and ex situ X-ray diffraction and X-ray computed tomography are used to conduct post-mortem analysis of electrodes after their first charge in the delithiated state. In doing so, the lattice changes and extent of cracking that occur in early operation are uncovered. The reversibility of these effects is assessed through comparison to discharged cathodes undergoing a full cycle and have been relithiated. Comparisons to pristine lithiated electrodes show an increase in cracking for all electrodes as the voltage increases during delithiation, with the majority of cracks then closing upon lithiation.
 [DOI: 10.1149/1945-7111/ace130]

Manuscript submitted February 9, 2023; revised manuscript received April 17, 2023. Published July 14, 2023.

With the increasing rate of adoption of electric vehicles,[1] and the desire for longer driving range, there is an ever growing demand for high energy density lithium-ion batteries.[2,3] This is currently being achieved by using Ni-rich chemistries which offer increased capacity (NMC811 (Li ($Ni_{0.8}Mn_{0.1}Co_{0.1}O_2$) has a capacity of approximately 180 mAh g^{-1} when cycled to 4.3 V vs Li) as well as ethical and economic benefits of reduced Co content.[4–7]Since the capacity of NMC811 increases with the upper cutoff voltage, there is a desire to increase it; however, high voltage operation can cause degradation of the materials via mechanisms such as cracking and oxygen loss. It is therefore crucial to understand these mechanisms to enable high-voltage operation and increase the capacity of current state-of-the-art materials.[8,9]

Under standard operating conditions, NMC811 generally experiences accelerated degradation (but higher initial capacity) than its lower Ni NMC counterparts, suffering from particle cracking, phase transitions to spinel and rock salt phases which impede charge transfer,[10,11] and transition metal migration.[12,13] These mechanisms can severely impede the performance of the cell, leading to losses in capacity. Particle cracking is of particular interest, due to its feedback loop with multiple other degradation mechanisms. Once a crack is formed, and reaches the surface of a particle, electrolyte can penetrate the crack, and react with the freshly exposed surfaces. Upon doing so, a passivating rock-salt layer with increased impedance may be formed upon the newly exposed surface, accompanied by the release of lattice oxygen. As the rest of the particle delithiates, this surface does not change unit cell volume to the same degree as the rest of the particle, creating a region of compressive stress, leading to yet more cracking.[14]

Particle cracking is unavoidable[15] due to the strain developed throughout cycling. Polycrystalline NMC materials have a typical cathode morphology consisting of 10 μm spherical secondary particles made up of primary particles 1 μm or smaller. The cathodes' $R\bar{3}m$ structure is made up of alternating transition metal oxide and lithium layers. During charge, lithium is removed from the structure, and re-inserted upon discharge. Removal of lithium leads to an initial expansion in the *c* lattice parameter (parallel with the interlayer spacing in the crystal) due to electrostatic repulsion between transition metal oxide layers. Upon further removal of lithium (>∼80% state of charge), the structure collapses as the effective charge of the oxygen decreases. The *a* lattice parameter decreases for the whole duration of charge, due to the reduction in atomic radii of the transition metals. The anisotropic changes in *a* and *c* impart strain on the material which expedites issues such as crack formation. X-ray diffraction (XRD) has been used extensively to characterise this phenomenon.[16–22]

By increasing the upper cut-off voltage, more lithium ions can be removed from the structure, therefore increasing the capacity of the material. Unfortunately, for lithium rich layered transition metal oxide cathodes (such as NMC), removing more lithium from the structure leads to adverse consequences such as accelerated capacity fading resulting from physical effects such as expedited crack formation and structure collapse.[23] In traditional "polycrystalline" NMC materials, particles contain hundreds of primary particles that agglomerate into larger secondary particles. The boundaries of these primary particles are the location for inter-granular fracture. Within primary particles, intra-granular fracture is possible, especially at high voltages.[24] Other obstacles include selecting an appropriate electrolyte which will be stable at the higher cut-off potentials. Therefore, work needs to be done to optimise the operating conditions in order to both prolong cycle life and access a higher percentage of the theoretical capacity.[10,24]

Particle cracking has been extensively studied at end-of-life, using methods such as SEM,[25] high resolution X-ray computed tomography (CT),[26,27] and lower resolution X-ray CT.[14] There is often a trade-off in analysing cracking in battery materials between the resolution of imaging and the sample size, meaning statistical evidence of cracking is often difficult to obtain. More recently, researchers have developed new methodologies to analyse large datasets of cracked particles. For example, automatic crack detection algorithms,[28] classifying degree of damage,[29] and algorithms to detect defects earlier and with quantitative results.[30] All these studies aim to categorise the effects multiple cycles have on a particle's states-of-health, and link it to the capacity losses, via imaging in the lithiated state. However, it has recently been shown that even during the early stages of charging, cracks within particles are formed.[31] It is therefore important that diagnostics take place throughout the charging process, to understand how and when cracks develop, particularly at high voltages where stress is exerted on the cathode particles.

In this paper, two techniques were employed to investigate the crack behaviour of NMC811, both at a de-lithiated and lithiated

[=]Equal Contribution.
[z]E-mail: P.Shearing@ucl.ac.uk

state, in the first cycle. NMC811 was charged to varying voltage cut-offs (the highest being 5.0 V vs Li^+/Li) to induce cracking. The changes in lattice structure were measured using XRD and the presence of defects/cracks studied by X-ray CT at three imaging resolutions. Both qualitative and quantitative analysis of the X-ray CT was carried out through visual analysis, calculations of volume fractions and intensity tracking algorithms.[30] Through the combination of these methods, paired with the information obtained from the electrochemical data, a deeper understanding of crack formation has been developed, the severity of defects within each particle quantified, and the reversibility of these phenomenon assessed.

Results

Crystallographic degradation.—In this study, polycrystalline NMC811 cathodes with an active material loading of 10 mg cm^{-2} (NEI Corporation, Summerset, USA) were charged to a range of voltages. They were then studied ex situ with various techniques to in order to understand cracking at multiple length scales, as highlighted in Fig. 1. A pristine electrode was used as the control sample. Four further electrode samples were charged to 4.0, 4.2, 4.4 and 5.0 V at a rate of 0.02 C. By increasing the cutoff voltage, the maximum achievable capacity of the electrode was increased, with NMC811 reaching capacities of 146.73 mAh g^{-1} at 4.0 V, 187.42 mAh g^{-1} at 4.2 V, 212.02 mAh g^{-1} at 4.4 V and 259.49 mAh g^{-1} at 5.0 V, as can be seen in Fig. 2a. Finally, four electrodes were charged to the above voltages (4.0, 4.2, 4.4 and 5.0 V) and then discharged to 3.7 V before analysis.

Figure 2b shows the differential capacity analysis for each upper cut-off voltage of the NMC811 half cells. There first anodic peak at 3.8 V arises from a phase transition from a hexagonal phase (H1) to a monoclinic phase (M) for NMC. The small anodic feature around 4.0 V is associated with the phase transition from M to a new hexagonal phase (H2) with a further phase transition occurring at 4.2 V, from H2 to H3, a new hexagonal phase. The lower voltage onset of the H2-H3 phase transition has been frequently reported for Ni-rich cathode materials and is linked to the lattice collapse.[19,32,33] Most of the achievable capacity for the cathode material is obtained by the bottom of the anodic peak at ca. 4.3 V. Therefore, there is little capacity to be gained by increasing the voltage cut-off to 4.4 V, which will likely decrease the cycle life of the cell quite rapidly.[34]

However, when the voltage cut-off is increased to 5.0 V, two more anodic peaks become visible at ca. 4.8 and 5.0 V, in line with the relatively large capacity jump when cycling to 5.0 V. It is likely these peaks can be attributed to chemical oxidation of the electrolyte by oxygen release from the cathode, which begins at 4.3 V. The reversibility of the peaks could also indicate oxygen redox in the cathode bulk. Oxidation of the electrolyte also leads to gas production of CO_2 and CO which builds as the voltage is increased. This is detrimental to the cell's lifetime.[35]

X-ray diffraction was used as a method of validating the state of charge of the electrodes after they had been disassembled from the coin cells and exposed to air. For layered transition metal oxide cathodes with the space group, $R\bar{3}m$, the *c*-lattice parameter expands and contracts during (de)lithiation; therefore, the *c*-lattice parameter can be used as a proxy for state of charge, the change of which can also be calculated by the position of the characteristic (003) NMC peak.[20]

The *a* value also varies with state of charge, as it is proportional to the ionic radii of the transition metals. As lithium is removed from the structure during charging, the transition metals are oxidised to compensate for the loss of charge. This effect is much more discrete than the changes in in *c*. Figure 2 shows the XRD patterns obtained for the fresh electrode, the electrodes charged to 4.0, 4.2, 4.4, and 5.0. The coloured solid line represents the experimental data and the black dotted lines show the calculated fit. Samples were measured at top of charge for 4.0, 4.2, 4.4 and 5.0 V. The (003) peak initially shifts to lower $^\circ$ 2θ, indicative of unit cell expansion in the *c*-direction. At 4.2 V and above, the (003) peak shifts to higher $^\circ$ 2θ values, indicating lattice collapse. Table I shows the refined *a*-lattice parameters, c-lattice parameters and unit cell volume obtained for the NMC811 electrodes at different lithiation states.

All the electrodes maintained the $R\bar{3}m$ structure and the refined lattice parameters are as expected,[16] with *c* increasing up to 4.2 V, beyond which the lattice collapses. These results validate that disassembling the cells in a lithiated state does not alter their degree of lithiation. Since for $R\bar{3}m$ $a = b$, the volume of the unit cell can be calculated by $V = a^2c$. As the contraction in *c* is greater than the initial expansion in a, the unit cell contracts throughout lithiation, with a rapid decrease upon the collapse of *c* at high degrees of delithiation. Upon relithiating the electrode, the lattice parameters recover to a value almost the same as that of the pristine sample ($c =$ 14.216 Å pristine, $c =$ 14.198 Å after being discharged from 5 V).

Particle cracking.—X-ray CT has been carried out at three length scales, utilizing two instruments, achieving voxel resolutions of ca. 32 nm, 64 nm and 200 nm. As the resolution decreases, more particles can be studied, enabling greater statistical confidence in the results, as highlighted in Fig. 1.

Two particles, one at the pristine state, and one at 5.0 V have been imaged using nano-CT with a voxel size of 32 nm. Phase imaging was used to enable a better distinction between phases, and as can be seen in Fig. 3a there are significantly more cracks present in the delithiated particle.

Further visual analysis indicates that the majority of cracks are all pointing in a similar direction, towards the centre of the particle. This can be quantified by comparing the location of the crack, with respect to the origin, and the angle that the crack is travelling at. The crack location is calculated through marking the outermost part of a crack and calculating the angle between that point and the vertical plane. This gives an angular location of the crack. The direction the crack travels is then calculated using the outermost point, a vertical line, and the angle between the crack line and the vertical line. This is diagrammatically displayed in Fig. 3c. These two angles are then summed and subtracted from 180 degrees, giving a relative

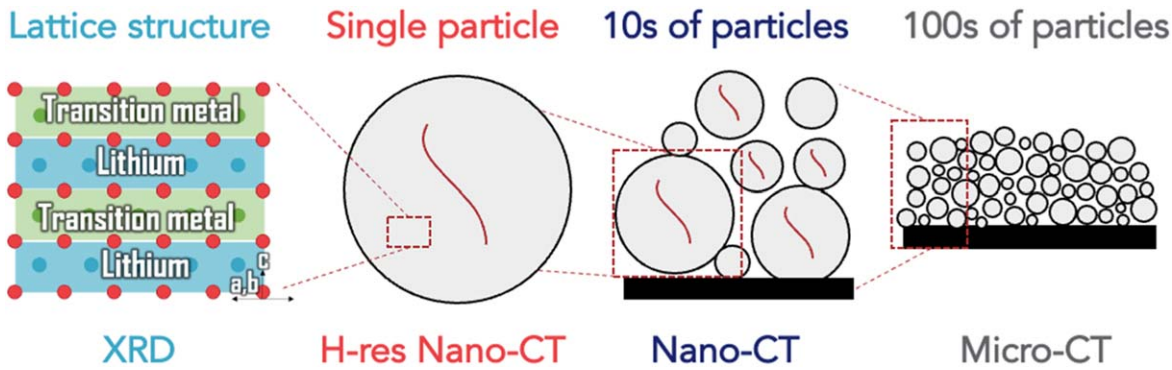

Figure 1. Multi-length-scale characterisation and corresponding features.

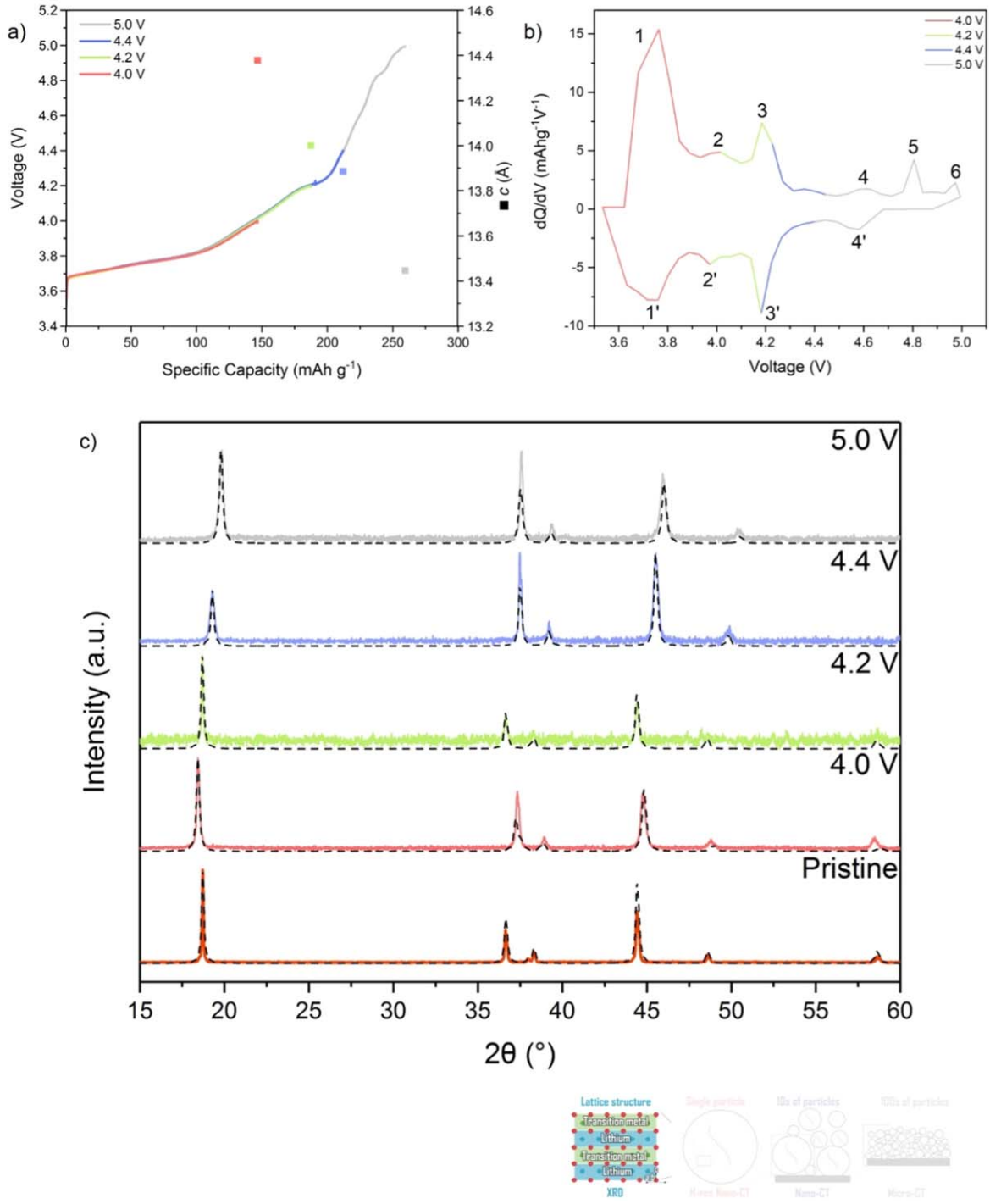

Figure 2. Degradation quantifications from electrochemistry and crystallography. (a) the specific capacity achieved for each cutoff voltage and the associated c-lattice parameter, (b) differential capacity curves for NMC811, (c) Refined diffraction patterns for each state of charge.

difference between the point and the crack direction. If the value is 0, then the crack is pointing directly at the centre of the particle. This is shown in Fig. 3c for over 20 cracks in the 5.0 V samples, taking cracks from the centre of all three orthogonal planes. The *y* axis, crack angle correction required, displays how many degrees the crack direction is from pointing directly at the centre, with the radial direction highlighting original angle where the crack has been taken from. From this, the majority of cracks are pointing towards the centre of the particle, with a single outlier in each plane.

Absorption contrast imaging has also been carried out, and the resulting scans have been cropped to remove the exterior pore space and segmented to active material and internal voids/cracks/defects. Particles in the lithiated and relithiated state have similar total volumes, Fig. 3d, confirming the particles are morphologically similar. The internal pore (voids/cracks/defects) volume is much larger for the 5.0 V sample, 258 μm^3 compared to 45.6 μm^3 for the pristine sample. This is further highlighted in the volume fractions in Fig. 3e, with the 5.0 V sample having a 21% pore fraction, compared to 3% from the pristine. Finally, a greyscale erosion algorithm[30] has been used on these particles, to compare the greyscale intensities of each particle through their respective radii. A lower value, caused by lower X-ray absorption, indicates the presence of voids or cracks. As

Table I. Refined lattice parameters obtained for NMC811 samples at different states of charge.

	Voltage cut-off during cycling		During data acquisition				
Name	Low	High	Voltage	Lithiation state	*a* (Å)	*c* (Å)	V (Å^3)
Pristine	N/A	N/A	N/A	Lithiated	2.873	14.216	101.609
4.0	N/A	4.0	4.0	Delithiated	2.823	14.427	99.547
4.2	N/A	4.2	4.2	Delithiated	2.822	14.249	98.689
4.4	N/A	4.4	4.4	Delithiated	2.819	13.800	94.942
5.0	N/A	5.0	5.0	Delithiated	2.813	13.446	92.166
4.0 discharged	3.0	4.0	3.7	Relithiated	2.863	14.133	100.358
4.2 discharged	3.0	4.2	3.7	Relithiated	2.866	14.197	101.173
4.4 discharged	3.0	4.4	3.7	Relithiated	2.862	14.135	100.302
5.0 discharged	3.0	5.0	3.7	Relithiated	2.868	14.198	101.194

seen in Fig. 3f, the 5.0 V sample has a decreased value towards the core of the particle, where the most voids are expected to be found due to the confluence of many radially oriented cracks.

Through both qualitative and quantitative analysis of these two scans, the particle at 5.0 V contains a larger proportion of defects than the pristine particle, with cracks primarily located in the core of the particle, with a direction towards the origin. However, this analysis covers only two particles (in two charge states); in the following two sections, lower resolution imaging (sampling a larger region of the electrode) is used to explore these findings and confirm the trends seen with a larger data set. Doubling the voxel size to 64 nm in nano CT still enables direct visualization of each particle, and thus any defects can be identified and a state-of-health for each particle qualitatively found.

As can be seen in 4b, the pristine particles are largely intact, apart from a selection of particles that have experienced cracking due to calendaring.[14] As the particles are taken to 4.0 V (Fig. 4c), several cracks appear, particularly among the large particles. Once the cell has reached 4.2 V, there are significant cracks within the particles present, several of which reach the surface of the particles. This increased separation between primary particles will likely enable electrolyte penetration into the interior of the particles and could also lead to electrical isolation of parts of the secondary particle. At 4.4 V (Fig. 4e), the cracking appears to be slightly less severe, potentially due to more homogeneous primary particle SoC and therefore homogeneous expansion. Finally, when the particles are most delithiated, the cell at 5.0 V, Fig. 4f, the cracks appear most severe, especially for the larger particles.

The visual condition of particles after discharging back to their lower voltage limit (3.7 V) is generally vastly different compared to their delithiated states (Figs. 4g–4j). Aside from defects likely due to calendaring during manufacture, the majority of particles appear to be in a good condition, with most cracks having closed significantly. This indicates that the separation observed at the top of charge is not only reversible but is likely caused by anisotropic expansion of primary particles as they delithiate. The exception here, during the visual analysis is the electrode at 5.0 V, which displays at least two particles still containing cracks in the ortho-slices displayed.

Since the high-resolution data is unlikely to be representative of the full electrode, the absolute volume fraction is unhelpful. However, a crack filling operation (fill internal volumes) has been carried out across all samples using Avizo software, which involves assigning all internal porosity (pores and cracks) to the particle that surrounds it. This results in segmented particles that contain both the active material and crack phases, and the volume fraction for these particles through the whole electrode are calculated. Finally, the volume fractions of the original and closed volumes are subtracted from one another, giving the volume fraction of cracks present and is displayed as a percentage (Fig. 4k). Across all electrodes, the delithiated samples show a significantly higher crack volume fraction when compared to the pristine or lithiated counterparts, confirming the visual analysis of crack opening and closing throughout cycling. However, this analysis is insufficient to determine the extent of damage, since the closing operation only works on internal voids, and therefore will undoubtedly miss larger cracks within particles.

To improve the statistical significance of the volume analysed, micro-CT has also been conducted. Combining the micro-scale X-ray CT data (Fig. 5a), with a recently developed greyscale analysis algorithm,[30] enables direct comparisons between electrodes and a wider understanding of the particle integrity. The methodology and operating procedure is explored in detail elsewhere.[30] A radial intensity profile for every particle in each sample has been calculated, and this value is normalised to its own surface value. As voids or cracks are less dense than active material, a region with cracks present is likely to have a lower intensity value, and a normalised intensity value below 1. Due to the number of particles analysed (1000 s per sample), they have been split into discrete bounds based on their size (radius), and intensity values within each bound averaged at each radial position. This enables the radial intensity of an average particle to be plotted, as has been done for all samples, with selected size bounds displayed in Figs. 5b–5e. In this figure, moving down the rows shows data for a sample cycled to a greater cut-off voltage.

The largest particles, (Fig. 5b, above 7 um) display some of the largest variations from the pristine baseline. This is in line with previous analysis, showing larger particles are more prone to cracking, due to greater SoC heterogeneity, and thus variations in volume changes. Samples from the 5.0 V cell have the lowest intensities, followed by 4.2 V, 4.0 V and finally 4.4 V. This is in line with the visual analysis above, and confirms that all electrodes experience some level of increased damage due to the lithium extraction, and 4.4 V large particles appear to contain fewer defects compared to samples taken to 4.2 and 5.0 V. For the same particle size group, there is also the largest variation between the pristine and relithiated (hollow spheres) intensities. Despite the intensity increasing compared to values at the top of each samples charge profile and showing crack-closing, there is still a difference between pristine and relithiated. This indicates that the cracking is not fully reversible for the largest particles, and there are still cracks present.

For the smaller particle bounds (6.0–7.0 μm, 5.0–6.0 μm and 3.5–4.0 μm) a similar trend is observed, with particles displaying cracks/defects when delithiated, and these cracks/defects closing when lithiated (and appearing to more fully close than those of the largest particles in the electrode). There are some exceptions, notably particles between 3.5–4.0 μm for the 4.0 V sample, showing very limited damage. However, despite the larger values, the slope of the line here, decreasing after a surface layer, suggest that some damage is present even within this sample set, which has caused the rapid reduction in intensity (not observed in the pristine samples for the same scale).

Finally, the percentage of particles within each size bound that has a normalized intensity below 1 (defects are present) is shown in Fig. 5f. The trend is the same as above, with higher voltage leading

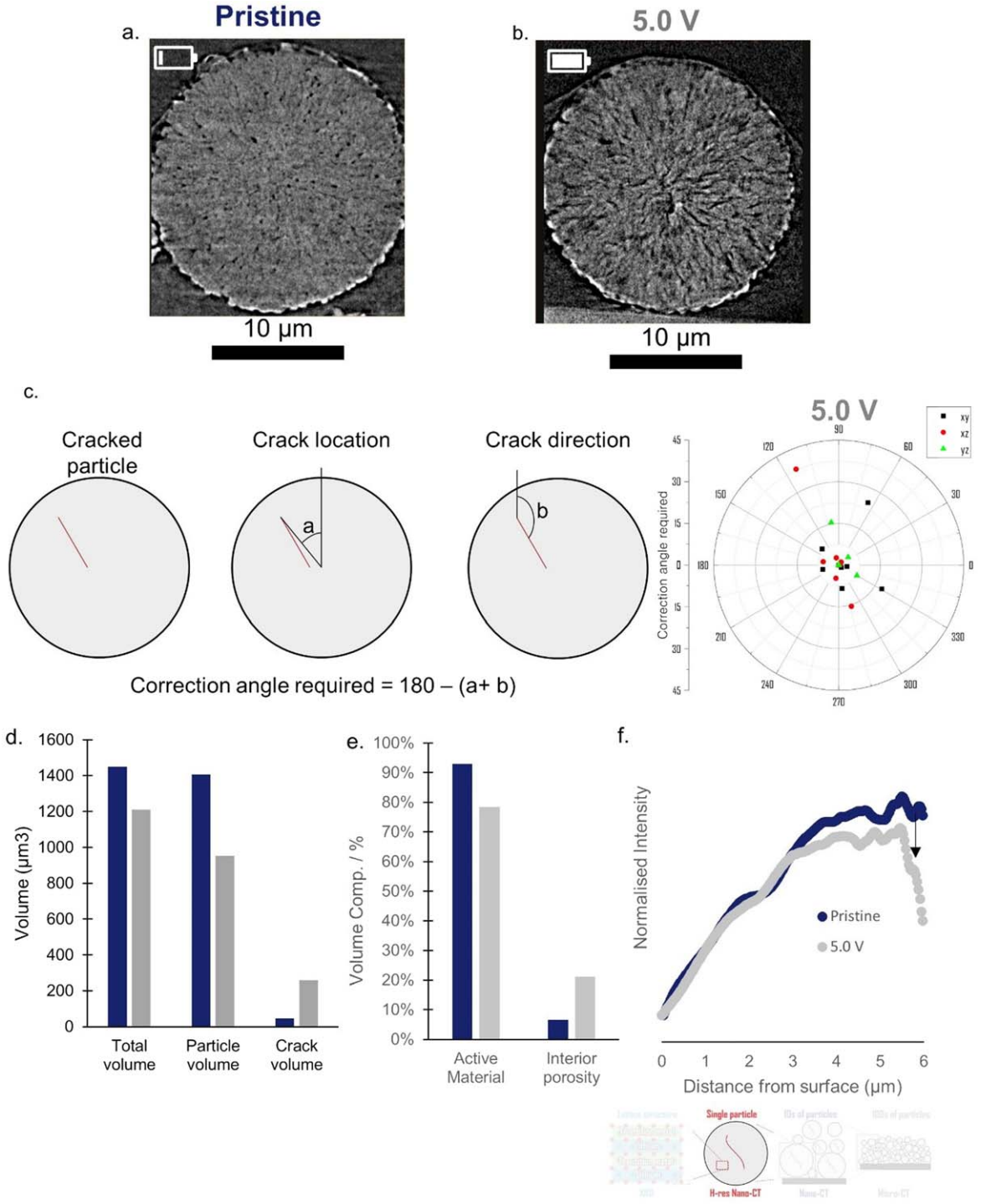

Figure 3. Degradation of secondary particles. high resolution CT slice of a pristine particle (b) high resolution CT slice of a particle at 5.0 V (c) crack angle calculation and crack angles in relation to their position for particle at 5.0 V (d) Volumes of both particles (e) volume fraction for both samples (f) interior greyscale values as a function of radius.

to widespread cracking for 4.0 V, 4.2 V and 5.0 V samples, with 4.4 V samples being more resistant, but still significantly more cracked than their relithiated counterpart. As particle size decreases, the 4.4 V particles display high levels or cracking, alongside high levels from all delithiated samples. When comparing the full spectrum of particle sizes (5f), there is a clear increase in the number of particles experiencing cracking when imaged at the upper cut-off voltages.

Multi-length scale imaging has revealed the same major trends within particles; cracks open up when charging and are most extensive at 4.2 and 5.0 V, and these cracks are concentrated in the centre of the particle, where they are likely to originate from. During relithiation, all samples display a significant level of crack closing, with larger particles more likely to still contain cracks.

Discussion

As discussed above, the diffraction results can be used to verify that the electrodes retain their state of charge in air for ex situ

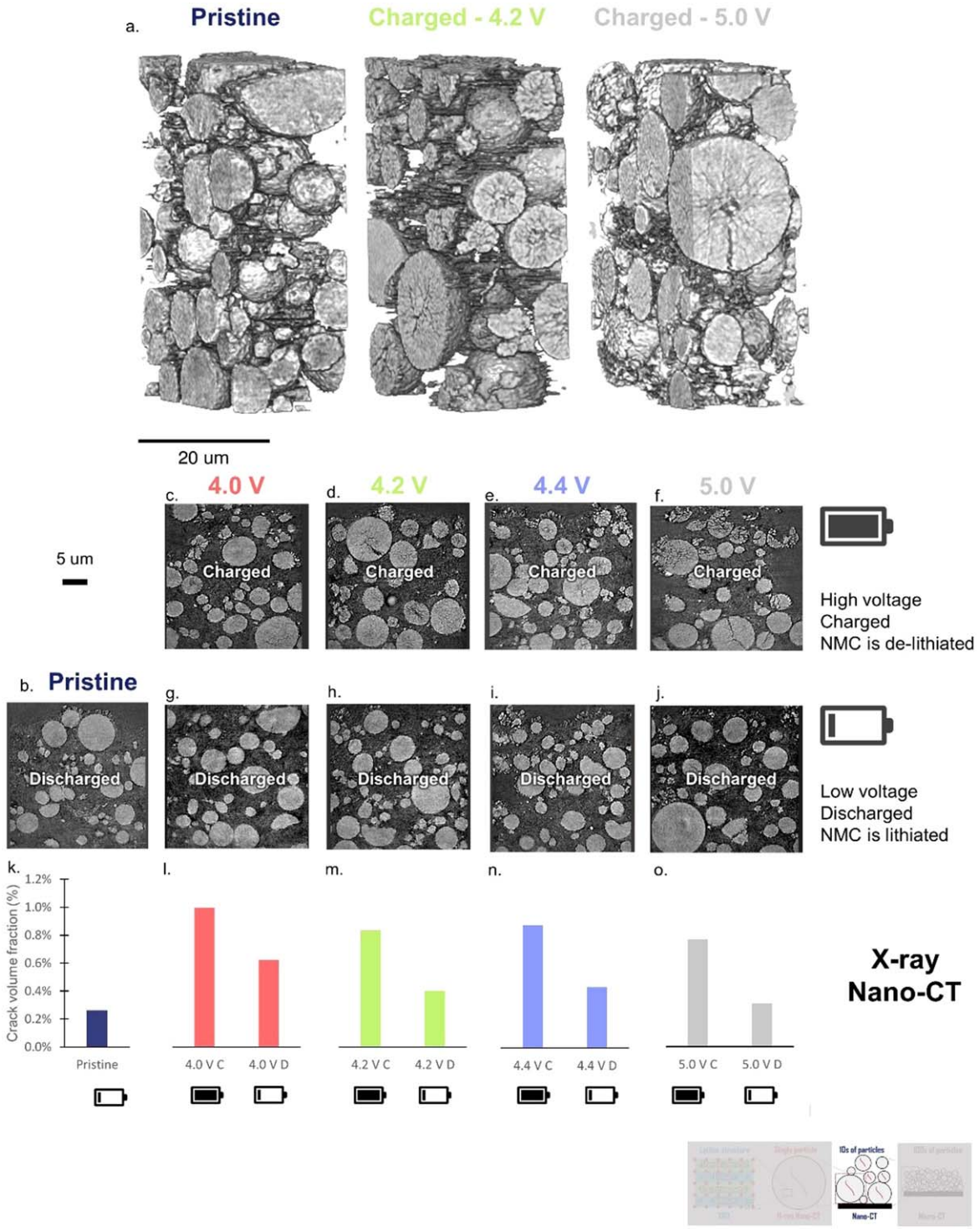

Figure 4. Localised electrode degradation. (a) 3D volume rendering extracted from pristine, delithiated 4.2 V and delithiated 5.0 V samples. Slices from nano-CT data for (b) Pristine (Lithiated), (c) 4.0 V (d) 4.2 V (e) 4.4 V (f) 5.0 V (g) 4.0 V relithiated (h) 4.2 V relithiated (i) 4.4 V relithiated (j) 5.0 V relithiated (k-o) cracks volume fractions for each sample.

analysis. As is well known upon charging, the unit cell lattice undergoes a large anisotropic contraction in the *c* direction at high states of delithiation. This can cause strain in the material and lead to cracking of the NMC particles, expediting subsequent degradation. Upon increasing the voltage, this contraction increases, causing further strain in the NMC and propagating extensive cracking as evidenced by the X-ray CT results.

It has also been shown that there during early charging there is a lithium concentration gradient across the particle, with a lithium-rich core and lithium-poor periphery. The lithium-poor periphery has a higher lithium diffusivity, accelerating the delithiation in this region. The boundary between the two regions propagates towards the core of the particle as charging progresses. This concentration gradient will result in a difference in *c*-lattice parameters across the particle, leading to stress/strain within the particle and subsequently mechanical degradation such as cracking, which has been imaged in this paper. This lithiation heterogeneity is more pronounced at the beginning of delithiation.[36]

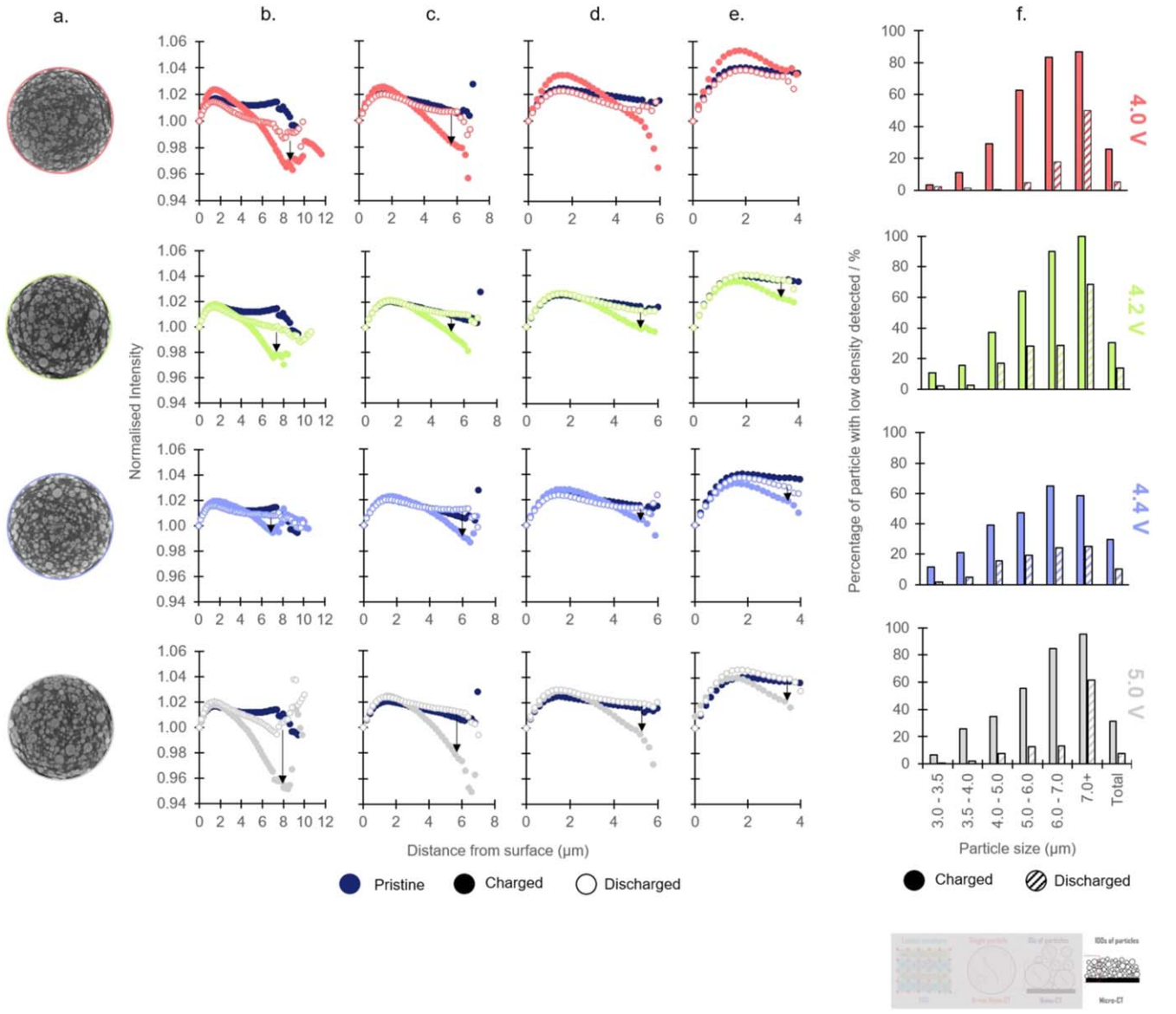

Figure 5. Bulk electrode degradation. Micro-CT quantification results where hollow spheres are relithiated and filled are delithiated, (a) slices from micro-CT data at each voltage, average normalized intensity for particles with radii (b) larger than 7.0 μm (b) between 6.0 and 7.0 μm (c) between 5.0 and 6.0 μm (d) between 3.5 and 4.0 μm (e) average normalized intensity for the particle core (f) percentage of cracked particles within each size bound for each sample.

In general, more cracks are present at the higher states of delithiation, where the lattice has collapsed more and there is the largest volume change, highlighted by 4.2 V, and 5.0 V all containing the highest percentage of cracked particles. However, as shown by XRD elsewhere,[16] an electrode is likely to contain particles at different lithiation states. This is the hypothesised reason as to why cracking is observed even at 4.0 V. At this voltage, the c lattice has not collapsed on a global scale, but a volume change is observed. However, if sufficient particles have undergone lattice changes, these individual particles are likely to be in a similar state to those at 4.2 V (cracked). This can be seen in the nano-CT data set, and in the analysis carried out through micro-CT and the quantification algorithm. The electrode is significantly more cracked than pristine (25.5% vs 6.8%), which is unlikely to be caused solely due to manufacturing defects.

When increasing the voltage to 4.4 V and 5.0 V, most particles would be expected to have undergone a collapse in the c lattice. However, at 4.2 V there is likely to be a larger SoC gradient within particles, with this equilibrating at 4.4 V, and thus generating less stress between particles.[36] This is highlighted by the dQ/dV curve, 4.2 V is the epicentre of the H2-H3 phase transition, linked to the unit cell collapse. At 4.2 V the NMC particles could therefore be in an extremely stressed state, with some particles undergoing the collapse at different rates, leading to anisotropic unit cell volume changes and extensive particle cracking. There are no further phase transitions observable in the dQ/dV when cycling to 4.4 V, so it is likely by the time the NMC reaches that potential, most of the particles have undergone the lattice collapse and thus there is less heterogeneity across the secondary particles and electrode.

Upon charging to extremely high voltages (5.0 V) the electrodes appear to be shattered with visible gaps between each primary particle. X-ray CT results detail the random grain orientations within the secondary polycrystalline particles. This is likely to exacerbate cracking during cycling as each individual grain non-uniformly lithiates and de-lithiates, eventually leading to gaps in the active material at extremely high voltages, where there is large unit cell contraction. Furthermore, two further peaks are observed in the dQ/dV data, due to the oxidation of the electrolyte due to oxygen

release. It is hypothesised that this oxygen release causes further cracking within the electrode, contributing to the shattered appearance visible in the nano-CT data.[37,38]

Upon discharging the electrodes, it can be seen both in the XRD and X-ray CT data that the electrodes tend to recover to a near-pristine state, for samples delithiated below 5.0 V. This solidifies the link between the unit cell contraction/expansion and cracking as both can be seen to be reversible during cycling. As this work is all performed in the first cycle it is expected that the reversibility of these reactions is at its optimum and will decrease with aging, as is also evidenced by the fact that it takes several hundreds of cycles to see significant degradation in these materials, therefore suggesting that the majority of first cycle cracking should be reversible. The only electrode where this may not be the case is the 5.0 V, which has cracked not only due to stress of volume changes but due to the oxygen release. A particle size distribution is shown in the supplementary data for the 5.0 V delithiated and 5.0 V relithiated samples. The relithiated data has a significantly higher percentage of small particles compared to the lithiated. This may be due to several large particles being irreversibly split into two smaller particles and detected as such, and the cracking percentage for the electrode is lower than expected. This phenomenon would also explain why the lower resolution imaging is unable to detect these cracks, since the particles are split into two and are therefore measured as two intact particles. This could be confirmed through future in situ work, and the visualisation of the same particles' behaviour throughout the cycling process. Furthermore, despite large particles showing lower crack closing, the electrode contains only a handful of these particles, compared with the hundreds of smaller particles, which undergo a higher degree of crack closing.

Overall, it is unlikely that 5.0 V will ever be a recommended operating voltage for lithium-ion batteries using NMC811 electrodes, due to the expedited degradation that would take place upon further cycling and the stability window of current battery electrolytes. However, this paper adds to the understanding of crack formation and the intrinsic link it has to the unit cell volume of the active material. It also shows the reversibility of these cracks in the first cycle, unseen before at such high voltages, and offers confidence that increased voltage cut-offs (between 4.4 V and 5.0 V) will not introduce irreversible cracking. Future work will include in situ tomography methods to allow for the same volume to be studied at all states of charge and therefore observe the same cracks throughout a full cycle of the electrode. Aged samples will also be studied, with a particular interest on the degree of reversibility versus the state of health of the electrode. This data can also be used to substantiate electro-mechanical modelling to determine how the formation of cracks in the first cycle might affect lifetime and performance. Furthermore, ex situ studies will talk place to confirm the presence of SoC heterogeneity within particles, alongside high-resolution microscopy to determine if larger particles contain larger pre-existing cracks than smaller particles. Finally, additional cycling to elevated voltages (5.0 V) will enable a clearer picture of the potential oxygen loss, additional cracking, and peaks observed in the differential capacity data.

Table II. Voxel size and cropped dimensions for micro-CT samples (1 d.p.).

	Status	Voxel size (nm)	Cropped dimension (μm)
Pristine	lithiated	199.5	163.8 × 190.1 × 39.9
4.0 V	relithiated	161.8	96.9 × 96.9 × 32.2
	delithiated	197.0	150.9 × 129.0 × 36.0
4.2 V	relithiated	200.8	142.8 × 110.2 × 33.9
	delithiated	200.8	121.9 × 158.0 × 49.0
4.4 V	relithiated	187.0	153.8 × 147.8 × 45.8
	delithiated	196.7	143.8 × 168.3 × 38.3
5.0 V	relithiated	199.9	129.7 × 120.1 × 50.2
	delithiated	200.1	127.4 × 137.2 × 50.2

Conclusions

In this work we have assessed NMC811 cathodes at multiple SOCs during their first cycle of operation. Through XRD analysis, the unit cell contraction has been observed, and matches with the SOC of the particles. Multi-length X-ray CT has enable both qualitative and quantitative analysis of the state-of-health of the particles. Cracks are present even at low voltages (4.0 V), and become more severe at 4.2 V and 5.0 V. At 4.4 V, in larger particles' cracks seem less severe, potentially due to SOC homogeneity across the electrode and particles, with smaller particles still experiencing significant cracking. Upon relithiation, all samples have shown cracks to close, signifying a reversibility to the volume expansion; however, due to electrolyte infiltration, it is expected that performance on subsequent cycles would be hampered for the most severely cracked particles.

Methods

Cell assembly and cycling.—CR-2025 type coin cells were assembled in an argon filled glovebox, adopting 15 mm discs of NMC811 (NEI NANOMYTE® BE-50E cast NMC811 (active material 90 weight %)) as the cathode and lithium metal as the counter electrode. The electrolyte used was LP57 (1 M solution of $LiPF_6$ in EC/EMC = 3/7 (v/v)) and was chosen due to its lack of additives, which can be unstable at the higher potentials used in this experiment. Celgard separator was also used (2400; Celgard, Tokyo, Japan). Samples were cycled using a BioLogic BCS805 coin cell cycler and were delithiated to various upper cutoff voltages using a low current of 0.02 C (C/50) to ensure as little overpotential as possible. Coin cells were then disassembled in an Argon filled glovebox where the electrodes were washed in dimethyl carbonate (DMC) and left to dry before exposing them to air for ex situ analysis.

XRD.—X-ray diffraction was performed on a Rigaku SmartLab SE utilising a 2 kW copper source Cu $K_{\alpha 1}$ and $K_{\alpha 2}$ (λ = 1.541 &1.544 Å) operating in Bragg-Brentano mode. Scans were carried out in a 2θ range of 15°–60° with a step size of 0.01° and a speed of 1.0 °min^{-1}. Samples were measured on a zero-background silicon wafer sample holder. Raw data files were converted to GSAS file format using the PowDLL convertor.[39] The refinements were then carried out using GSAS-II software[40] on an EXPGUI graphical interface.[41]

X-ray CT information.— *Micro-scale.*—Micro X-ray CT was conducted using a Versa 520 X-ray instrument (Zeiss Xradia 520 Versa, Carl Zeiss., CA, USA) employing an accelerating tube voltage of 80 kV_p and a stationary tungsten anode on a copper substrate that produces a polychromatic beam with a characteristic emission peak at 58 keV (W-Kα). For all samples, an exposure time of 45 s was used, with a power of 8 Watts. 1601 projections were used for all samples, except for 4.0 V, where 1561 projections were taken.

After imaging, the 2D radiographs were reconstructed into 3D tomogram using "Reconstructor Scout-and-Scan," (Carl Zeiss, Ca, U.S.A), using cone-beam filtered-back-projection (FBP) algorithms. This produced tomograms with a voxel length of ca. 200 nm (Table II). Visualization and segmentation of the tomograms was completed in Avizo Fire (Avizo, Thermo Fisher Scientific, Waltham, Massachusetts, U.S.A.). To reduce the effect of artefacts on the segmentation process, internal sub-volumes of each scan were taken, with the sizes displayed in Table II. The active material, NMC811 was segmented into on phase, and the pore and binder were segmented into a second phase. To aid in segmentation and remove noise, non-local means or gaussion filters were used when necessary.

Nano-scale.—Nano-scale X-ray CT was conducting using an Ultra 810 X-ray instrument (Zeiss Xradia 520 Versa, Carl Zeiss., CA, USA), in both large-field-of-view (LFOV) and high-resolution

(HRes) modes. This instrument uses a quasi-monochromatic 5.4 kEV, parallel beam geometry, with a chromium anode. All scans were completed at 35 keV, and at a power of 0.9 kW. Imaging was carried out in both absorption and Zernike phase contrast modes were used, with absorption mode used for calculations and phase contrast used for illustration.

For LFOV imaging, a camera binning of 1 was used for all samples, giving an isotropic voxel size of 65 nm, post reconstruction. For the absorption scans an exposure time of 60 s, with 1201 projections was used. For phase contrast imaging, the exposure time was 30 s, with 1201 projections.

For single particle imaging, the Ultra 810 HRes mode was used, with a camera binning of 2, with an exposure time of 90 s and X projections. Post reconstruction, all HRes scans had a voxel size of 32 nm. Nano-scale data reconstruction was completed using "Reconstructor Scout-and-Scan," (Carl Zeiss, Ca, U.S.A.), via FBP algorithms. Visualization and segmentation of the tomograms was completed in Avizo Fire (Avizo, Thermo Fisher Scientific, Waltham, Massachusetts, U.S.A.). The active material, NMC811 was segmented into one phase, and the pore and binder were segmented into a second phase. To aid in segmentation and remove noise, non-local means or gaussion filters were used when necessary.

Acknowledgments

This work was carried out with funding from the Faraday Institution (faraday.ac.uk; EP/S003053/1) Degradation, Multiscale Modelling and SAFEBATT projects, grant numbers FIRG001, FIRG003, FIRG024, FIRG025, FIRG028, FIRG060 and FIRG061. The authors would like to acknowledge the Royal Academy of Engineering (CiET1718\59) for financial support. Use of the instruments was supported by EP/N032888/1.

Data Processing

The volume fractions for each phase were calculated in Avizo Fire, using the segmented tomograms. When completing radial intensity analysis, the GREAT algorithm and its accompanying workflow was employed. This involved running the algorithm, sorting the results into size bounds, averaging the intensity at each point and plotting the new "average particle."

Data Availability

All data is available upon request from the corresponding author.

Author Contributions

A.W. and A.L. both author contributed equally as co-first authors. A.L., A.W., C.T. and T.H. conceived the study. A.L. prepared the coin cells, A.L. and C.T. electrochemically cycled the coin cells. A.L. harvested samples from the coin cells and performed the XRD. A.W. and A.L. prepared the X-ray CT samples and performed all X-ray imaging. A.W. and T.H. processed the X-ray data. R.J. is the FIRG001/024/060 project lead. D.B., R.J and P.S. directed and sourced funding for all work. All authors aided in the preparation of the manuscript.

Competing Interests

The Authors declare no Competing Financial or Non-Financial Interests.

ORCID

A. Wade https://orcid.org/0000-0003-1713-5617
A. V. Llewellyn https://orcid.org/0000-0003-1071-3824
T. M. M. Heenan https://orcid.org/0000-0001-9912-4772
Rhodri Jervis https://orcid.org/0000-0003-2784-7802
P. R. Shearing https://orcid.org/0000-0002-1387-9531

References

1. L. Lu, X. Han, J. Li, J. Hua, and M. Ouyang, "A review on the key issues for lithium-ion battery management in electric vehicles." *J. Power Sources*, **226**, 272 (2013).
2. A. Manthiram, "An outlook on lithium ion battery technology." *ACS Cent Sci*, **3**, 1063 (2017).
3. M. G. Boebinger, J. A. Lewis, S. E. Sandoval, and M. T. Mcdowell, "Understanding transformations in battery materials using in situ and operando experiments: progress and outlook." *ACS Energy Lett.*, **5**, 335 (2019).
4. A. Manthiram, J. C. Knight, S. T. Myung, S. M. Oh, and Y. K. Sun, "Nickel-rich and lithium-rich layered oxide cathodes: progress and perspectives." *Adv. Energy Mater.*, **6**, 1501010 (2016).
5. S. T. Myung et al., "Nickel-rich layered cathode materials for automotive lithium-ion batteries: achievements and perspectives." *ACS Energy Lett.*, **2**, 196 (2017).
6. J. Kim et al., "Prospect and reality of Ni-Rich cathode for commercialization." *Adv. Energy Mater.*, **8**, 1 (2018).
7. T. C. Frankel, "The cobalt pipeline." *The washington Post* (2022).
8. V. Etacheri, R. Marom, R. Elazari, G. Salitra, and D. Aurbach, "Challenges in the development of advanced Li-ion batteries: a review." *Energy Environ. Sci.*, **4**, 3243 (2011).
9. Y. Mao et al., "High-voltage charging-induced strain, heterogeneity, and micro-cracks in secondary particles of a nickel-rich layered cathode material." *Adv. Funct. Mater.*, **29**, 1 (2019).
10. W. Xue et al., "Ultra-high-voltage Ni-rich layered cathodes in practical Li metal batteries enabled by a sulfonamide-based electrolyte." *Nat. Energy*, **6**, 495 (2021).
11. N. Laszczynski, S. Solchenbach, H. A. Gasteiger, and B. L. Lucht, "Understanding electrolyte decomposition of graphite/NCM811 cells at elevated operating voltage." *J. Electrochem. Soc.*, **166**, A1853 (2019).
12. H. Zheng, Q. Sun, G. Liu, X. Song, and V. S. Battaglia, "Correlation between dissolution behavior and electrochemical cycling performance for LiNi 1/3Co 1/ 3Mn 1/3O 2-based cells." *J. Power Sources*, **207**, 134 (2012).
13. D. R. Gallus et al., "The influence of different conducting salts on the metal dissolution and capacity fading of NCM cathode material." *Electrochim. Acta*, **134**, 393 (2014).
14. T. M. M. Heenan et al., "Identifying the origins of microstructural defects such as cracking within Ni-Rich NMC811 cathode particles for lithium-ion." *Batteries.*, **10**, 2002655 (2020).
15. H. Li et al., "An unavoidable challenge for Ni-Rich positive electrode materials for lithium-ion batteries." *Chem. Mater.*, **31**, 7574 (2019).
16. A. S. Leach et al., "Spatially resolved operando synchrotron-based X-ray diffraction measurements of Ni-Rich cathodes for li-ion batteries." *Frontiers in Chemical Engineering*, **3**, 1 (2022).
17. A. K. C. Estandarte et al., "Operando bragg coherent diffraction imaging of $LiNi_{0.8}Mn_{0.1}Co_{0.1}O_2$ primary particles within commercially printed NMC811 electrode sheets." *ACS Nano*, **15**, 1321 (2021).
18. C. Tian, F. Lin, and M. M. Doeff, "Electrochemical characteristics of layered transition metal oxide cathode materials for lithium ion batteries: surface, bulk behavior, and thermal properties." *Acc. Chem. Res.*, **51**, 89 (2018).
19. C. Xu et al., "Bulk fatigue induced by surface reconstruction in layered Ni-rich oxide cathodes for Li-ion." *Batteries. ChemXRiv*, **20**, 1 (2020).
20. C. Xu, P. J. Reeves, Q. Jacquet, and C. P. Grey, "Phase behavior during electrochemical cycling of Ni-Rich cathode materials for li-ion batteries." *Adv. Energy Mater.*, **2003404**, 1 (2020).
21. K. Rhodes, R. Meisner, Y. Kim, N. Dudney, and C. Daniel, "Evolution of phase transformation behavior in Li(Mn1.5Ni0.5)O4 cathodes studied by In Situ XRD." *J. Electrochem. Soc.*, **158**, A890 (2011).
22. S. R. Daemi et al., "Exploring cycling induced crystallographic change in NMC with X-ray diffraction computed tomography." *Phys. Chem. Chem. Phys.*, **22**, 17814 (2020).
23. L. Mu et al., "Oxygen release induced chemomechanical breakdown of layered cathode materials." *Nano Lett.*, **18**, 3241 (2018).
24. P. Yan et al., "Intragranular cracking as a critical barrier for high-voltage usage of layer-structured cathode for lithium-ion batteries." *Nat. Commun.*, **8**, 14101 (2017).
25. B. Song et al., "Nano-structural changes in Li-ion battery cathodes during cycling revealed by FIB-SEM serial sectioning tomography." *J Mater Chem A Mater*, **3**, 18171 (2015).
26. T. M. M. Heenan et al., "4D nano-tomography of electrochemical energy devices using lab-based X-ray imaging." *Nano Energy*, **47**, 556 (2018).
27. X. Lu et al., "3D microstructure design of lithium-ion battery electrodes assisted by X-ray nano-computed tomography and modelling." *Nat. Commun.*, **11**, 1 (2020).
28. L. Petrich et al., "Crack detection in lithium-ion cells using machine learning." *Comput. Mater. Sci.*, **136**, 297 (2017).
29. Y. Yang et al., "Quantification of heterogeneous degradation in Li-Ion batteries." *Adv. Energy Mater.*, **9**, 1900674 (2019).
30. A. Wade et al., "A greyscale erosion algorithm for tomography (GREAT) to rapidly detect battery particle defects." *Npj Mater Degrad*, **6**, 44 (2022).
31. P. C. Tsai et al., "Single-particle measurements of electrochemical kinetics in NMC and NCA cathodes for Li-ion batteries." *Energy Environ. Sci.*, **11**, 860 (2018).
32. R. Jung, M. Metzger, F. Maglia, C. Stinner, and H. A. Gasteiger, "Oxygen release and its effect on the cycling stability of $LiNi_xMn_yCo_zO_2$(NMC) cathode materials for Li-Ion batteries." *J. Electrochem. Soc.*, **164**, A1361 (2017).
33. K. Marker, P. J. Reeves, C. Xu, K. J. Griffith, and C. P. Grey, "Evolution of structure and lithium dynamics in $LiNi_{0.8}Mn_{0.1}Co_{0.1}O_2$ (NMC811) cathodes during electrochemical cycling." *Chem. Mater.*, **2**, 2545 (2019).

34. C. Mao et al., "Evaluation of gas formation and consumption driven by crossover effect in high-voltage lithium-ion batteries with Ni-Rich NMC cathodes." *ACS Appl. Mater. Interfaces*, **11**, 43235 (2019).
35. R. Jung, M. Metzger, F. Maglia, C. Stinner, and H. A. Gasteiger, "Chemical versus electrochemical electrolyte oxidation on NMC111, NMC622, NMC811, LNMO, and conductive carbon." *J. Phys. Chem. Lett.*, **8**, 4820 (2017).
36. C. Xu et al., "Operando visualization of kinetically induced lithium heterogeneities in single-particle layered Ni-rich cathodes." *Joule*, **6**, 2535 (2022).
37. S. Sharifi-Asl, J. Lu, K. Amine, and R. Shahbazian-Yassar, "Oxygen release degradation in Li-Ion battery cathode materials: mechanisms and mitigating approaches." *Adv. Energy Mater.*, **9**, 1900551 (2019).
38. W. Dose et al., "Onset potential for electrolyte oxidation and Ni-rich cathode degradation in lithium-ion batteries." *ChemRxiv*, **2**, 3524 (2022).
39. N. P. D. L. L. Kourkoumelis, *Powder Diffr.*, **28**, 137 (2013).
40. A. C. Larson and R. B. Von Dreele, "General structure analysis system (GSAS)." *Los Alamos National Laboratory Report LAUR*, 86 (1994).
41. B. H. Toby, "EXPGUI." *Applied Crystallography*, **34**, 210 (2001).